Ultrafast shift current dynamics in WS_2 monolayer

Fuxiang He,[1,2] Daqiang Chen,[3] Xinguo Ren,[3,*] Sheng Meng,[3] and Lixin He[1,2,†]

[1]*Key Laboratory of Quantum Information, University of Science and Technology of China, Hefei, Anhui 230026, People's Republic of China*

[2]*Synergetic Innovation Center of Quantum Information and Quantum Physics, University of Science and Technology of China, Hefei 230026, People's Republic of China*

[3]*Beijing National Laboratory for Condensed Matter Physics, Institute of Physics, Chinese Academy of Sciences, Beijing 100190, China*

(Received 8 July 2022; revised 20 August 2023; accepted 3 January 2024; published 30 January 2024)

The shift current effect, in materials lacking inversion symmetry, may potentially allow the performance of photovoltaics to surpass the Shockley-Queisser limit for traditional *p-n* junction-based photovoltaics. Although the shift-current effect has been studied from first principles via second-order perturbation theory, an understanding of the dynamics of hot carriers is still lacking. We investigate the dynamics of the shift current in monolayer WS_2 via real-time propagation time-dependent density functional theory (rt-TDDFT). We find that the shift current can be generated within 10–20 fs after turning on the lights, and dissipates within approximately a few tens of femtoseconds after turning off the lights. This property can be used for ultrafast photon detection. This work provides an important step toward understanding the dynamics of shift-current effects, which is crucial for device applications.

DOI: 10.1103/PhysRevResearch.6.013123

I. INTRODUCTION

In materials lacking inversion symmetry, current can be generated under illumination, which is known as the bulk photovoltaic effect (BPVE) or "shift current" effect [1–3]. The direction of the generated current can be reversed via external voltages as demonstrated in the $BiFeO_3$ single crystal [4]. The shift current effect (or the BPVE) can be used as an alternative to the photocurrent generated by traditional semiconductor *p-n* junctions [5,6]. More remarkably, it allows the generation of a photovoltage far above the band gap [7–9]. For example, the measured open-circuit voltage in BFO can be as large as 30 V, ten times larger than its band gap of ∼2.7 eV [10]. It therefore may potentially allow the performance of the BPVE-based photovoltaics to surpass the Shockley-Queisser limit for the traditional *p-n* junction based photovoltaics [11].

The shift-current effect is a nonlinear optical response [3,12]. It is now understood that the shift current originates from the change in the Berry connection of electron bands upon optical transition [13,14]. Recently the shift-current conductivity has been calculated via first-principles methods [15–19], which may provide useful guidance to find suitable materials for PV and other applications [6].

Despite intensive investigations over the past decades, the understanding of the shift current is far from complete. Even though the shift-current has been studied via model Hamiltonians [20–22], a quantitative investigation of the dynamics of excited "hot" carriers through first-principles calculations is still lacking. It has been shown that PV conversion efficiency is closely related to the diffusion length and carrier relaxation time [11,23]. To achieve high efficiency, it is crucial to understand the carrier dynamics to optimize PV devices.

In this work, we investigate the shift-current dynamics in monolayer WS_2 using the real-time propagation time-dependent density functional theory (rt-TDDFT) [24–27], which is a powerful tool for investigating time-dependent effects in nonlinear optical processes [28–30]. We examine the influence of temperature on the excitation and dissipation of the shift current. We show that the shift current can be established within 10–20 fs after turning on the light and diminishes on a similar time scale when the light is turned off, which can be used for ultrafast photon detection. Our work provides an important step to understanding the dynamics of shift currents from first-principles calculations.

II. METHODS

A. Calculation of shift current via rt-TDDFT method

The shift-current conductivities have been calculated via a second-order perturbation theory [12]. In this work, we calculate the photonexcited current directly via time-dependent wave functions. The current density $\boldsymbol{J}(t)$ under the light field is given by

$$\boldsymbol{J}(t) = \frac{e\hbar}{m}\sum_{n=1}^{\mathrm{occ}}\sum_{\boldsymbol{k}}\mathrm{Im}[\langle\tilde{\psi}_{n\boldsymbol{k}}(t)|\nabla|\tilde{\psi}_{n\boldsymbol{k}}(t)\rangle], \tag{1}$$

where $\tilde{\psi}_{n\boldsymbol{k}}(t)$ is the time-dependent Bloch wave function of the nth band at point $\boldsymbol{k}$. The time-dependent wave functions

*renxg@iphy.ac.cn
†helx@ustc.edu.cn

are obtained by the real-time evolution of the time-dependent Kohn-Sham equation, under an external time-dependent electric field $\boldsymbol{E}(\omega, t)$.

To be compatible with the periodic boundary conditions, a velocity gauge is used for the electric field [31], i.e.,

$$\boldsymbol{E}(\omega, t) = -\frac{1}{c}\frac{\partial \boldsymbol{A}(\omega, t)}{\partial t}. \tag{2}$$

The vector potential is taken to be uniform in the system, i.e.,

$$\boldsymbol{A}(\omega, t) = \boldsymbol{A}_0 \cos(\omega t)\,. \tag{3}$$

The time-dependent Kohn-Sham equation under the vector potential reads [31]

$$i\hbar\frac{\partial}{\partial t}\tilde{\psi}_i(t) = \left\{\frac{1}{2m}\left[\boldsymbol{p} + \frac{e}{c}\boldsymbol{A}(t)\right]^2 + \hat{\tilde{V}}^{\text{eff}}(t)\right\}\tilde{\psi}_i(t)\,, \tag{4}$$

where $\hat{\tilde{V}}^{\text{eff}}(t) = V_{Hxc}[n(t)] + \hat{\tilde{V}}_{\text{ion}}$, with $V_{Hxc}[n(t)]$ being the time-dependent Hartree-exchange-correlation potential, and $\hat{\tilde{V}}_{\text{ion}}$ the electron-ion interaction operator under the vector potential [31]. For simplicity, we neglect the real-space symbol $\boldsymbol{r}$ in the equation. We solve Eq. (4) via real-time evolution of the wave function using the Crank-Nicholson scheme [25].

B. Computational details

The shift current of the WS_2 monolayer is simulated via the rt-TDDFT methods implemented in the atomic orbital based *ab initio* computation at USTC (ABACUS) package [32]. ABACUS is developed to perform large-scale density functional theory (DFT) calculations based on numerical atomic orbitals (NAO) [33]. We adopt the Perdew-Burke-Ernzerhof (PBE) exchange-correlation functional [34] and the SG15 [35] optimized norm-conserving Vanderbilt (ONCV) pseudopotentials [36] are used to describe the interactions between ions and valence electrons. The DFT-D3 correction of Grimme [37] is used to describe the van der Waals interactions. A uniform real-space grid corresponding to an energy cutoff of 240 Ry for the charge density is adopted to solve the Poisson equation via fast Fourier transform. The $2s2p1d$ NAO basis set for S, and the $4s2p2d2f$ basis set for W are used to expand the Kohn-Sham wave functions. The cutoff radii of the NAOs are set to 10 a.u.

We simulate the monolayer WS_2 supercell containing $4\times4\times1$ primitive cells, and a 17 Å vacuum is added to avoid interaction between the periodic images. A $24\times24\times1$ $\boldsymbol{k}$-mesh (which is equivalent to a $96\times96\times1$ $\boldsymbol{k}$-mesh for the unit cell) is used to sample the Brillouin zone, which converges the results very well. The time step for the electron wave function evolution is set to 0.05 fs. To study the temperature effects and the electron-phonon interactions, we also perform the Ehrenfest molecular dynamics (MD) [38] for the ions along with the electron wave function evolution.

The linearly polarized lights are used in our simulations, and due to the time-reversal symmetry of WS_2, only the shift currents are observable, while the injection currents are excluded [12]. To isolate the shift current from the total currents, we average the calculated currents over a 50 fs period once they stabilize. In the rising and decaying stages, an averaging period of 1 fs is used. This effectively removes the rapidly oscillating linear order current and ensures robust convergence of the results. Additional information regarding the calculation and reliability validation is available in Appendix A.

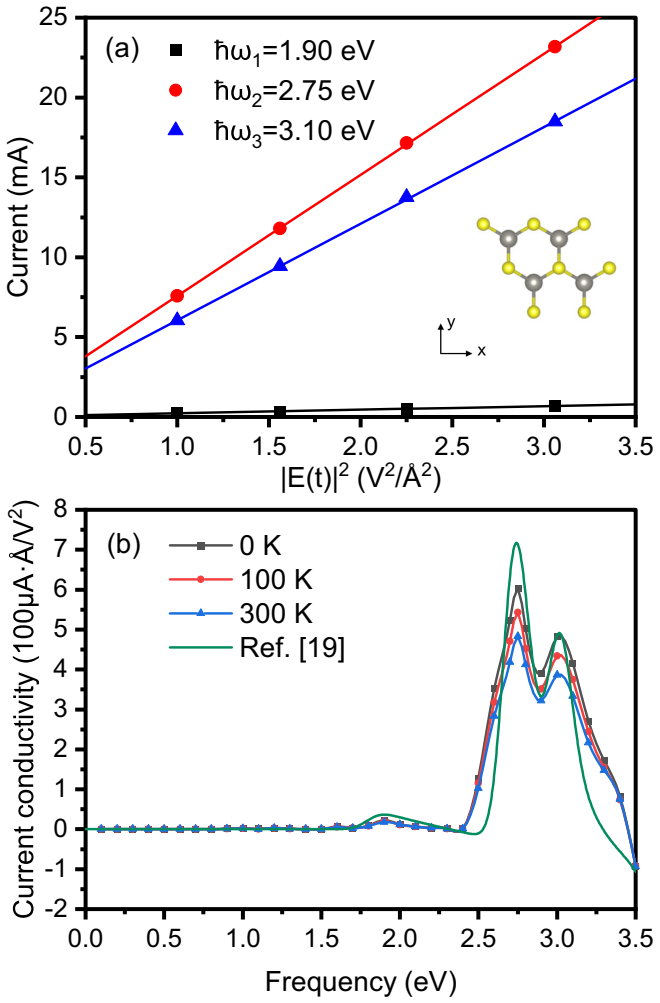

FIG. 1. (a) The calculated shift currents (scatters) under different light intensity for $\hbar\omega = 1.9$ eV, 2.75 eV, and 3.1 eV, demonstrating an excellent linear fit with $|E|^2$ (solid lines). The insert shows the structure of monolayer WS_2. (b) Shift current conductivities σ^{yyy} as functions of excitation energy at 0 K, 100 K, and 300 K, respectively. The conductivity calculated by the perturbation theory from Ref. [19] is also shown as a comparison.

III. RESULTS AND DISCUSSION

We first investigate the shift-current conductivities $\sigma^{\alpha\beta\beta}(\omega)$ of monolayer WS_2 [19]. We calculate the shift currents at each frequency ω under different excitation powers. Since a periodic boundary condition is used in our simulation, it is equivalent to simulating infinitely stacked WS_2 layers, which differs from the single-layer setup used in Refs. [39,40].

Figure 1(a) depicts the shift currents as functions of the excitation power for photon energies $\hbar\omega = 1.9$ eV, 2.75 eV, and 3.1 eV at zero temperature. The numerically calculated shift currents increase linearly with the excitation power, and the shift current conductivity can be fitted very well accordingly

using the following relation [3]:

$$J^{\alpha} = \sigma^{\alpha\beta\beta}(\omega)E^{\beta}(\omega)E^{\beta}(-\omega)\,, \tag{5}$$

where α and β are the lattice directions.

The fitted conductivity $\sigma^{yyy}(\omega)$ as a function of the excitation energy at $T = 0$ K is shown in Fig. 1(b). There are two major peaks: the first peak is at approximately 2.75 eV, with $\sigma^{yyy} = 0.60$ mA·Å/V^2, and the second peak is at approximately 3.1 eV, with $\sigma^{yyy} = 0.48$ mA·Å/V^2. There is also a very weak peak at approximately 1.9 eV. The calculated current along the x axis is zero conductivity due to the mirror symmetry $\hat{M}^y$, and therefore σ^{xxx} and σ^{xyy} are zero [17,19]. The conductivities calculated at $T = 0$ K in this work are in good agreement with the previous results obtained by a second-order perturbation theory method [17,19], considering the results are from two very different approaches. This is not surprising because the shift-current conductivity is determined by the geometries of the energy band structures [13–15]. However, the conductivities obtained through rt-TDDFT exhibit slightly greater smearing compared to those calculated from perturbation theory. This broadening of peaks in the TDDFT simulation can be attributed to electron-electron scattering resulting from the temporal evolution of the Hartree-exchange-correlation potentials. In contrast, the smearing in perturbation theory is governed by an artificial parameter.

Thus far, we have reproduced the shift-current conductivity of previous calculations. However, this method can go beyond the previous perturbation theory, and allows us to calculate the shift current at finite temperatures. In these calculations, the dynamics of ions are described by the classical MD. The shift-current conductivities at 100 K and 300 K are also shown in Fig. 1. For the excitation energy $\hbar\omega = 2.75$ eV, σ^{yyy} decreases from 0.60 mA·Å/V^2 at $T = 0$ K, to 0.54 mA·Å/V^2 at 100 K, and 0.48 mA·Å/V^2 at 300 K. Similarly, for $\hbar\omega = 3.1$ eV, σ^{yyy} decreases from 0.48 mA·Å/V^2 at $T = 0$ K to 0.44 mA·Å/V^2 at $T = 100$ K, and 0.39 mA·Å/V^2 and 300 K. The shift-current conductivity gradually decreases with the increasing of temperature, presumably due to electron-phonon scattering.

To further analyze the contribution to the shift current, we project the time-dependent wave functions $\tilde{\psi}_{nk}(t)$ to KS orbitals $\tilde{\psi}^0_{mk}$ of the ground state, i.e., the KS orbitals before applying the excitation light,

$$|\tilde{\psi}_{n\boldsymbol{k}}(t)\rangle = \sum_m c_{nm,\boldsymbol{k}}(t)\big|\tilde{\psi}^0_{m\boldsymbol{k}}\big\rangle\,, \tag{6}$$

where m is the band index of the ground state Kohn-Sham orbitals. The shift current can then be written as

$$\langle\tilde{\psi}_{n\boldsymbol{k}}(t)|\nabla|\tilde{\psi}_{n\boldsymbol{k}}(t)\rangle = \sum_{m,m'} c^*_{nm,\boldsymbol{k}}(t)c_{nm',\boldsymbol{k}}(t)\big\langle\tilde{\psi}^0_{m\boldsymbol{k}}\big|\nabla\big|\tilde{\psi}^0_{m'\boldsymbol{k}}\big\rangle\,. \tag{7}$$

We find that the shift currents calculated via Eq. (7) are almost identical to the original results. The major contribution to the shift currents in the studied energy range comes from the highest occupied bands and the lowest unoccupied bands, which are consistent with previous work [19].

The total shift current can be decomposed into the off-diagonal contribution, i.e., the contribution from $m \neq m'$ terms, and the diagonal contribution, i.e., the $m = m'$ terms. We can further decompose the diagonal contribution from electrons (i.e., m sum over the unoccupied bands) and holes (i.e., m sum over the occupied bands). The diagonal terms are related to the quantity $\Delta_{mn}(\boldsymbol{k}) = v_{mm}(\boldsymbol{k}) - v_{nn}(\boldsymbol{k})$, where $v_{mm}(\boldsymbol{k})$ and $v_{nn}(\boldsymbol{k})$ are the velocities of the electrons and holes, respectively [12,18]. Δ_{mn} has a clear physical meaning that this part of the shift current arises from the electron velocity change on the optical transition. Note that the observed contribution is not from the injection current, which is absent in this system [12]. Please refer to Appendix B for a detailed explanation.

TABLE I. The total shift currents (in mA), along with the off-diagonal and diagonal currents, in single-layer WS_2. The excitation power is 1.33×10^{13} W/cm^2, at $T = 0$ K.

Frequency	Total current (mA)	Off-diagonal (mA)	Diagonal (mA)
2.75 eV	7.57	0.35	7.22
3.10 eV	6.03	0.73	5.30

Table I lists the total shift currents and the off-diagonal and diagonal components for $\hbar\omega = 2.75$ eV and 3.10 eV. As we see from the table, the shift current is dominated by the diagonal contribution. For $\hbar\omega = 2.75$ eV, off-diagonal contribution accounts for only roughly 5% of the total current, and the other 95% is contributed by the diagonal current. Similar results are also obtained for the $\hbar\omega = 3.10$ eV case. The diagonal current contributes 88% of the total current, whereas the off-diagonal term only contributes 12%. Whether this is a general result for other materials remains to be further studied.

One of the most prominent advantages of the rt-TDDFT method is that it can explore the ultrafast dynamics of the process. It is interesting to see how fast the system can establish steady shift current under illumination. Figure 2 shows the shift current as a function of time after turning on the laser with $\hbar\omega = 2.75$ eV. As one can see, the shift current

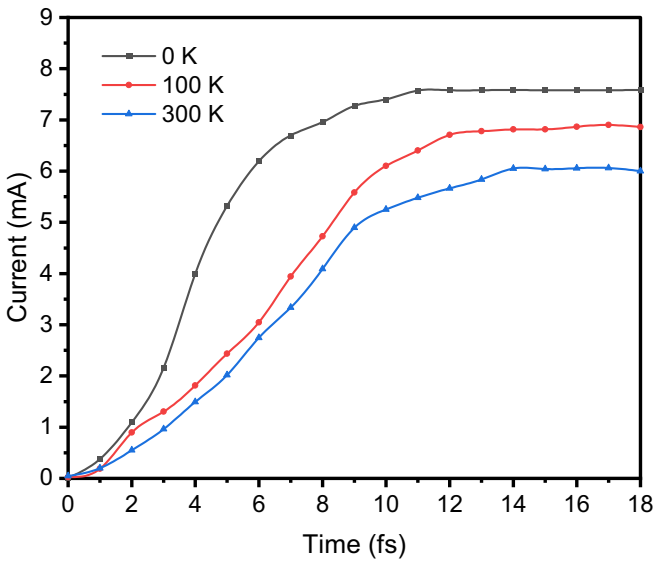

FIG. 2. The generation of shift currents after turning on the light with the excitation of 1.0×10^{10} W/cm^2 at 0 K, 100 K, and 300 K, respectively.

TABLE II. Lifetimes of shift currents and their components at different temperatures with photo energy $\hbar\omega = 2.75$ eV.

Temperature	Total current (fs)	Electron (fs)	Hole (fs)
0 K	21.84	17.71	20.40
100 K	19.39	13.36	20.33
300 K	17.84	11.08	15.85

quick raises after applying the laser, and the saturation times of the shift current after excitation are about 11 fs, 12 fs, and 14 fs at temperatures of 0 K, 100 K, and 300 K, respectively. This suggests that the shift-current effect can be used as ultrafast photon detectors, whereas the typical response time for photodiode based photon detectors is about a few tens of picoseconds. Figure 2 reveals that at the same excitation power, the saturated shift currents at 100 K is 89% of that at 0 K, whereas the saturated shift currents at 300 K is only about 80% of that at 0 K. This could be understood that at higher temperatures, the electron-phonon scattering is stronger, therefore the generated shift current would be weaker. Similar results are obtained for the $\hbar\omega = 3.10$ eV. In order to investigate whether the excitation power influences the saturation current and current dynamics, we performed calculations using three distinct incident light intensities and the results are presented in Fig. 8 of Appendix A. These results indicate that the magnitudes and dynamics of the shift currents remain consistent across the three different excitation intensities.

After turning off the lights, the shift current would dissipate. The dissipation time of the shift current, which determines the diffusion length of the excited carriers, is crucial for the PV device applications [11]. To calculate the current relaxation time, we turn off the light after the current becomes steady, and monitor the decay of the current. Figures 3(a)–3(c) depict the decay of the shift current after turning off the light at 0 K, 100 K, and 300 K, respectively, at $\hbar\omega = 2.75$ eV. We show the results for the total currents, and the components including the electrons, holes, as well as the off-diagonal currents. The total shift current, electronic current, and hole current all decay (roughly) exponentially. Specifically, the electron currents decrease almost to zero at about 30–45 fs, depending on the temperature. However, the total currents and the hole currents have some (about 10% of the steady currents) long-lived residual components, which do not decay to zero in the simulated time range. Remarkably, the off-diagonal current only has small oscillations between 0.10 mA and 0.52 mA, and does not decay in the simulation up to 45 fs for all temperatures.

We further fit the current relaxation times of the total, electron, and hole currents at different temperatures via exponential functions, and the results are shown in Table II. The relaxation times of the shift currents decrease with increasing temperature, as expected, due to the stronger electron-phonon scattering. For the total shift current, the relaxation time decays from 21.84 fs at 0 K to 17.84 fs at 300 K. The relaxation times of electrons (around 11 fs–18 fs) are a little shorter than those of holes (around 15 fs–20 fs). The small long-life residuals of the total and hole currents cannot be fitted very

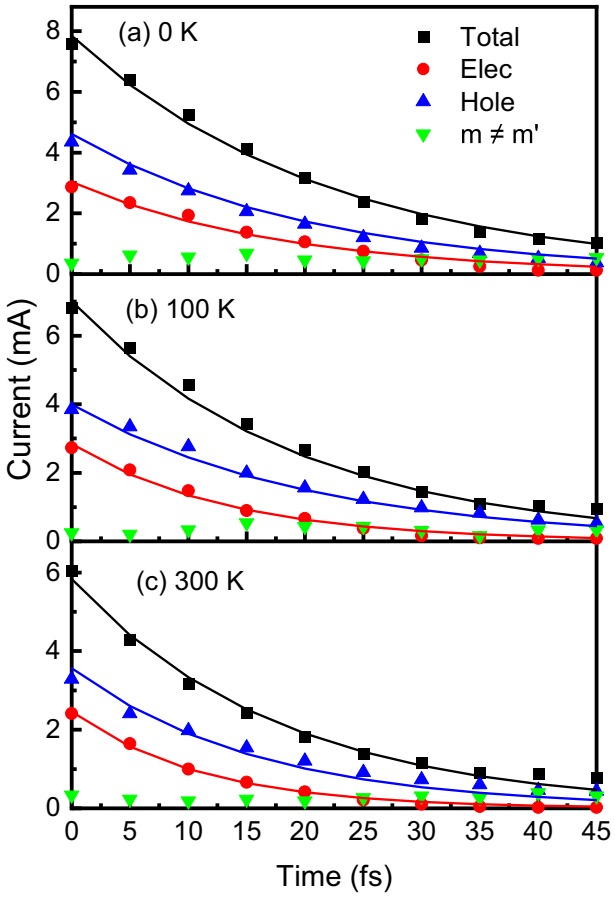

FIG. 3. The dissipation of the total, electron, hole, and off-diagonal ($m \neq m'$) currents at (a) 0 K, (b) 100 K, and (c) 300 K, respectively, after turning off the light field.

well due to the limited simulation time. In fact, the carrier relaxation times are not very sensitive to temperature, which reflects the band topological nature of the shift current [13].

It has been shown that long-range (LR) exchange interactions may play an important role in electron-electron scattering in semiconductors [41]. We conducted extra calculations with the long-range exchange-correlation functional [42,43], and the results are shown in Fig. 7 of Appendix A. The results align with those from the PBE functional, confirming that incorporating long-range exchange interactions doesn't change the fundamental results and conclusions of the paper.

We note that the relaxation times of the shift currents are not identical to the carrier lifetimes due to electron-phonon scattering or electron-impurity scattering, as the former ones are finite (and very short) even in perfect crystals at zero temperature. The ultrafast shift current relaxation times are probably due to electron-electron scattering. The diffusion length l_0 can be estimated as $l_0 \approx \tau \cdot v_k$. The very short current relaxation times are responsible for the extremely low BPV effects in bulk materials, because most photon generated hot carriers are relaxed before they reach the electrode [11]. However, when the distance between the electrodes is comparable to the diffusion length, the BPV effects are greatly enhanced [10,11,23,44]. The mechanisms of the shift-current

relaxation and the calculation of the diffusion length are extremely important for the applications, which are beyond the scope of this work. We leave them for future studies.

IV. SUMMARY

The dynamics of shift current are extremely important not only for fundamental science, but also for device applications. We investigate the shift current dynamics in the WS_2 monolayer by using the rt-TDDFT method. We find that the shift current can be established within 10–20 fs, and the current dissipates within approximately a few tens of femtoseconds. This property can be used for ultrafast photon detection. This work is an important step toward understanding the dynamics of shift-current effects.

ACKNOWLEDGMENTS

We thank Prof. Y. Xu for sharing their data of shift current conductivities with us. This work was funded by the Chinese National Science Foundation Grants No. 12134012, No. 11774327, No. 11874335, and No. 12188101. The numerical calculations were performed on the USTC HPC facilities.

APPENDIX A: ADDITIONAL CALCULATION DETAILS

In this section, we offer additional calculation details to underscore the reliability of our results.

Figure 4 compares the band structures of WS_2 calculated using the plane wave (PW) basis and the numerical atomic orbital (NAO) basis. It is evident that within the pertinent energy range, the band structures obtained by the two methods exhibit remarkable agreement with each other. These results suggest that our chosen NAO basis is sufficiently accurate for performing shift-current calculations on the system.

In this work, the forces are calculated using the full expression, which includes the Pulay forces. Details about the force calculations can be found in Ref. [32]. We have conducted examinations on the changes in total energy after the

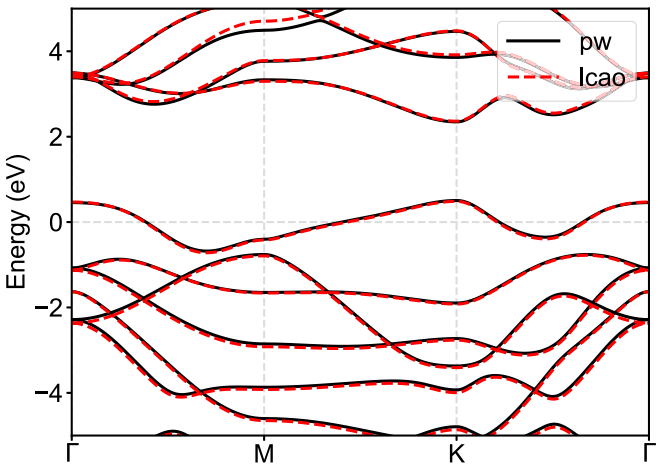

FIG. 4. Comparison of WS_2 band structures calculated using plane wave (PW) and numerical atomic orbital (denoted as LCAO) bases.

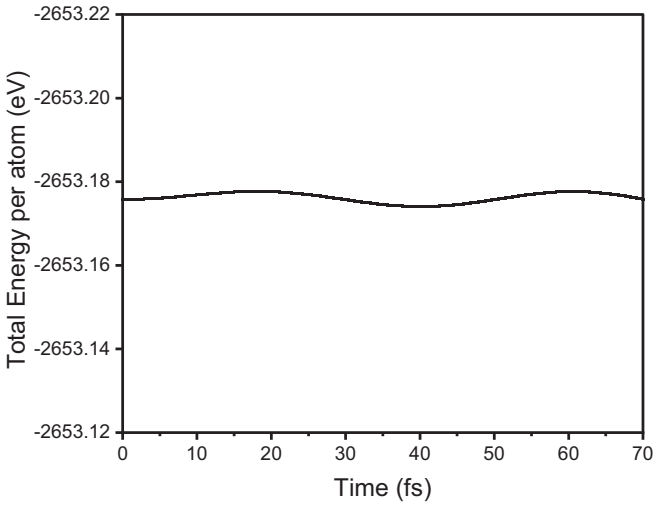

FIG. 5. Variation in the total energy of monolayer WS_2 after the cessation of light exposure.

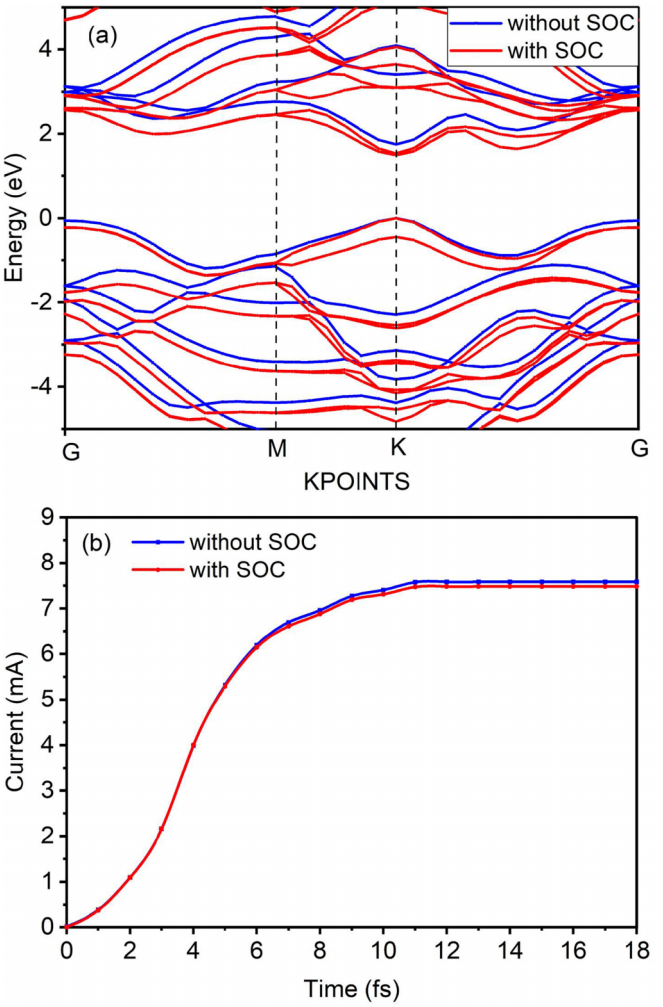

FIG. 6. (a) The energy band diagram of single-layer WS2 considering the spin orbit coupling effect or not. (b) Comparison of the effects of spin orbit coupling on the shift current of single-layer WS2 under optical field excitation.

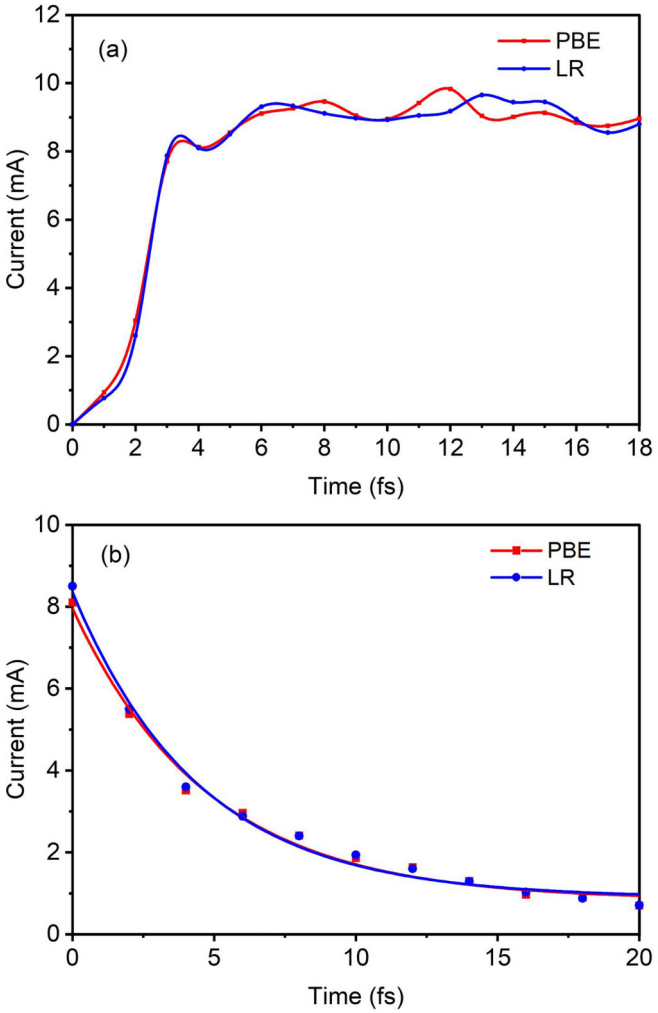

FIG. 7. Comparison of shift-current (a) generation and (b) decay in a single-layer WS_2 system using PBE and long-range (LR) exchange functionals.

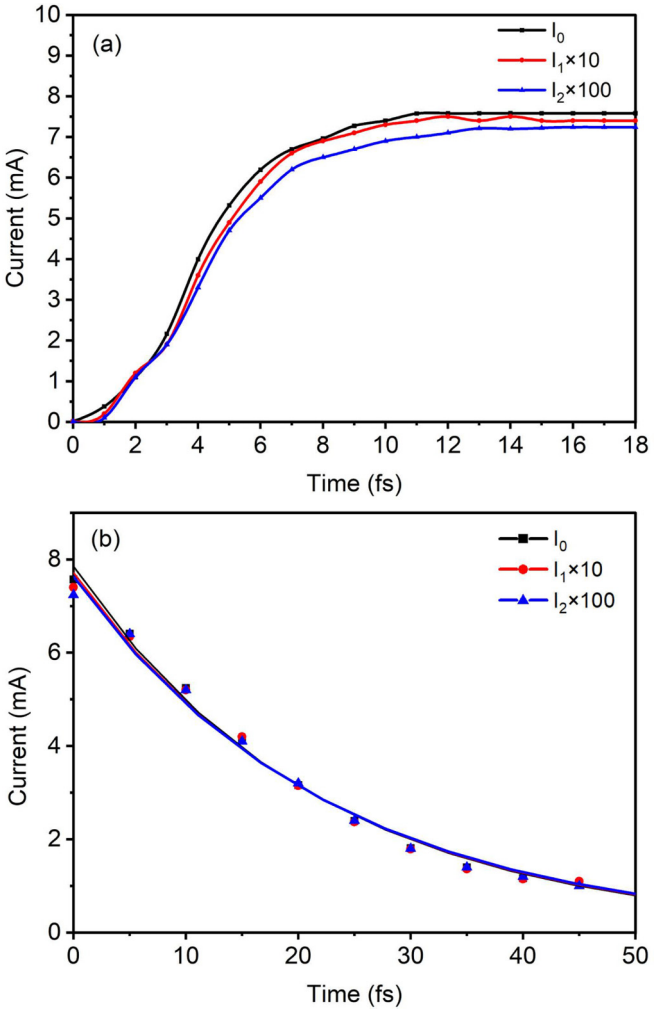

FIG. 8. (a) Comparison of shift current generation in a single-layer WS_2 under various excitation light intensities: $I_0 = 1.0\times10^{10}$ W/cm^2, $I_1 = I_0/10$, and $I_2 = I_0/100$. (b) Comparison of current attenuation for the currents generated by I_0, I_1, and I_2.

removal of the light field, and the results are depicted in Fig. 5. The results indicate that despite the presence of small short-term oscillations in the total energy, long-term stability in energy conservation is well maintained for up to 70 fs. This demonstrates the accuracy and reliability of our calculations throughout the entire simulation.

In order to assess the impact of spin-orbit coupling (SOC) effects, we compute the energy band structures of the monolayer WS_2 both with and without SOC. The results are presented in Fig. 6(a). Incorporating SOC does not significantly alter the band structures, except for a reduction in the band gap by 0.2 eV. We also performed calculations to investigate the excitation of the shift current with and without SOC, and the results are shown in Fig. 6(b). The results demonstrate that the dynamics of shift-current excitation remain nearly unchanged in the presence of SOC. Therefore, SOC has a minimal effect on the shift current dynamics, and in the main text of the paper, we only present results without SOC inclusion.

It has been shown that if the electronic interactions are described on the level of adiabatic PBE (local in time, semilocal in space), it might omit important channels of the electron-electron scattering in semiconductors [41]. To examine the impact of long-range (LR) exchange interactions on the dynamics of the shift current, we performed additional calculations using the long-range exchange-correlation functional [42,43], which explicitly accounts for these interactions. Unfortunately, the long-range exchange functional is not currently implemented in ABACUS [32], and therefore, we utilized the TDAP software [27] to obtain the results. As shown in Fig. 7, when incorporating the LR exchange interaction, the shift current generated by the laser field at 0 K exhibits saturation within approximately 6 fs and decay within approximately 20 fs. These results align with the findings obtained using the PBE functional. Therefore, including the long-range exchange interaction does not alter the fundamental results and conclusions of the paper. We note that there are some oscillations in the shift current calculated by the TDAP code, which is absent in the results of ABACUS code. This may be due to different implementation of the rt-TDDFT algorithm in the two codes. However, the overall results are

consistent to each other. Since the LR exchange-correlation functional is significantly more expensive than the PBE functional, we still use the PBE functional for the calculations in the main text.

In order to investigate whether the excitation power influences the saturation current and current dynamics, we performed calculations using three distinct incident light intensities: $I_0 = 1.0\times10^{10}$ W/cm^2, $I_1 = I_0/10$, and $I_2 = I_0/100$. The calculated shift currents are illustrated in Figs. 8(a) and 8(b). The results indicate that the magnitudes and dynamics of the shift currents remain consistent across the three different excitation intensities.

APPENDIX B: CONTRIBUTIONS TO SHIFT CURRENT

To gain insight into the results presented in the main text, we can draw comparisons with the shift-current conductivities obtained through second-order perturbation theory [12,18]. The relevant equations are as follows:

$$\sigma_{c;a,b}(0;\omega,-\omega) = -\frac{i\pi e^3}{2\hbar^2}\sum_{mn\boldsymbol{k}} f_{nm}\big(r^b_{mn}(\boldsymbol{k})r^a_{nm;c}(\boldsymbol{k}) + r^a_{mn}(\boldsymbol{k})r^b_{nm;c}(\boldsymbol{k})\big)\delta(\omega_{mn}-\omega), \quad \text{(B1)}$$

where $f_{nm} = f_n - f_m$ and $\hbar\omega_{nm} = E_n - E_m$ are differences between Fermi occupation factors and band energies, respectively. The dipole matrix r^a_{nm} and its generalized derivative $r^a_{nm;b}$ are calculated as follows [12,18] (here we drop the $\boldsymbol{k}$ index for simplicity),

$$r^a_{nm} = \frac{v^a_{nm}}{i\omega_{nm}} \quad (m \neq n), \quad \text{(B2)}$$

and

$$r^a_{nm;b} = \frac{i}{\omega_{nm}}\left[\frac{v^a_{nm}\Delta^b_{nm} + v^b_{nm}\Delta^a_{nm}}{\omega_{nm}} - w^{ab}_{nm} + \sum_{p\neq n,m}\left(\frac{v^a_{np}v^b_{pm}}{\omega_{pm}} - \frac{v^b_{np}v^a_{pm}}{\omega_{np}}\right)\right] (m \neq n), \quad \text{(B3)}$$

where

$$\begin{aligned} v^a_{nm} &= \frac{1}{\hbar}\langle u_{n\boldsymbol{k}}|\partial_a H(\boldsymbol{k})|u_{m\boldsymbol{k}}\rangle, \\ \omega_{nm} &= E_n - E_m, \\ \Delta^a_{nm} &= \partial_a\omega_{nm} = v^a_{nn} - v^a_{mm}, \\ w^{ab}_{nm} &= \frac{1}{\hbar}\langle u_{n\boldsymbol{k}}|\partial^2_{ab}H(\boldsymbol{k})|u_{m\boldsymbol{k}}\rangle. \end{aligned} \quad \text{(B4)}$$

As evident from Eq. (B3), the shift current includes a component originating from Δ_{mn}, representing the velocity difference between the valence and conduction bands. This component is closely linked to the diagonal contributions discussed in the main text. It is crucial to distinguish this contribution from the injection current, which also features a contribution from Δ_{mn}. In the context of this system, the injection current is absent due to the presence of time-reversal symmetry in WS_2, and linearly polarized light sources are employed. The remaining terms in Eq. (B3) represent contributions originating from the off-diagonal elements.

[1] A. G. Chynoweth, Surface space-charge layers in barium titanate, Phys. Rev. **102**, 705 (1956).

[2] V. M. Fridkin, A. A. Grekov, P. V. Ionov, A. I. Rodin, E. A. Savchenko, and K. A. Mikhailina, Photoconductivity in certain ferroelectrics, Ferroelectrics **8**, 433 (1974).

[3] B. I. Sturman and V. M. Fridkin, *The Photovoltaic and Photorefractive Effects in Noncentrosymmetric Materials*, 1st ed. (Routledge, London, 1992).

[4] T. Choi, S. Lee, Y. Choi, V. Kiryukhin, and S.-W. Cheong, Switchable ferroelectric diode and photovoltaic effect in $BiFeO_3$, Science **324**, 63 (2009).

[5] L. Z. Tan, F. Zheng, S. M. Young, F. Wang, S. Liu, and A. M. Rappe, Shift current bulk photovoltaic effect in polar materials—hybrid and oxide perovskites and beyond, npj Comput. Mater. **2**, 16026 (2016).

[6] A. M. Cook, B. M. Fregoso, F. de Juan, S. Coh, and J. E. Moore, Design principles for shift current photovoltaics, Nat. Commun. **8**, 14176 (2017).

[7] A. M. Glass, D. von der Linde, and T. J. Negran, High-voltage bulk photovoltaic effect and the photorefractive process in $LiNbO_3$, Appl. Phys. Lett. **25**, 233 (1974).

[8] G. Dalba, Y. Soldo, F. Rocca, V. M. Fridkin, and P. Sainctavit, Giant bulk photovoltaic effect under linearly polarized x-ray synchrotron radiation, Phys. Rev. Lett. **74**, 988 (1995).

[9] S. Y. Yang, J. Seidel, S. J. Byrnes, P. Shafer, C.-H. Yang, M. D. Rossell, P. Yu, Y.-H. Chu, J. F. Scott, J. W. Ager, L. W. Martin, and R. Ramesh, Above-bandgap voltages from ferroelectric photovoltaic devices, Nat. Nanotechnol. **5**, 143 (2010).

[10] M. Alexe and D. Hesse, Tip-enhanced photovoltaic effects in bismuth ferrite, Nat. Commun. **2**, 256 (2011).

[11] J. E. Spanier, V. M. Fridkin, A. M. Rappe, A. R. Akbashev, A. Polemi, Y. Qi, Z. Gu, S. M. Young, C. J. Hawley, D. Imbrenda, G. Xiao, A. L. Bennett-Jackson, and C. L. Johnson, Power conversion efficiency exceeding the Shockley–Queisser limit in a ferroelectric insulator, Nat. Photon. **10**, 611 (2016).

[12] J. E. Sipe and A. I. Shkrebtii, Second-order optical response in semiconductors, Phys. Rev. B **61**, 5337 (2000).

[13] T. Morimoto and N. Nagaosa, Topological nature of nonlinear optical effects in solids, Sci. Adv. **2**, e1501524 (2016).

[14] H. Hatada, M. Nakamura, M. Sotome, Y. Kaneko, and M. Kawasaki, Defect tolerant zero-bias topological photocurrent in a ferroelectric semiconductor, Proc. Natl. Acad. Sci. USA **117**, 20411 (2020).

[15] S. M. Young and A. M. Rappe, First principles calculation of the shift current photovoltaic effect in ferroelectrics, Phys. Rev. Lett. **109**, 116601 (2012).

[16] F. Zheng, H. Takenaka, F. Wang, N. Z. Koocher, and A. M. Rappe, First-principles calculation of the bulk photovoltaic

effect in $CH_3NH_3PbI_3$ and $CH_3NH_3PbI_{3-x}Cl_x$, J. Phys. Chem. Lett. **6**, 31 (2015).

[17] C. Wang, X. Liu, L. Kang, B.-L. Gu, Y. Xu, and W. Duan, First-principles calculation of nonlinear optical responses by Wannier interpolation, Phys. Rev. B **96**, 115147 (2017).

[18] J. Ibañez-Azpiroz, S. S. Tsirkin, and I. Souza, *Ab initio* calculation of the shift photocurrent by Wannier interpolation, Phys. Rev. B **97**, 245143 (2018).

[19] C. Wang, S. Zhao, X. Guo, X. Ren, B.-L. Gu, Y. Xu, and W. Duan, First-principles calculation of optical responses based on nonorthogonal localized orbitals, New J. Phys. **21**, 093001 (2019).

[20] T. Barik and J. D. Sau, Nonequilibrium nature of nonlinear optical response: Application to the bulk photovoltaic effect, Phys. Rev. B **101**, 045201 (2020).

[21] O. Matsyshyn, F. Piazza, R. Moessner, and I. Sodemann, Rabi regime of current rectification in solids, Phys. Rev. Lett. **127**, 126604 (2021).

[22] S. Rajpurohit, C. Das Pemmaraju, T. Ogitsu, and L. Z. Tan, Nonperturbative study of bulk photovoltaic effect enhanced by an optically induced phase transition, Phys. Rev. B **105**, 094307 (2022).

[23] A. Zenkevich, Y. Matveyev, K. Maksimova, R. Gaynutdinov, A. Tolstikhina, and V. Fridkin, Giant bulk photovoltaic effect in thin ferroelectric $BaTiO_3$ films, Phys. Rev. B **90**, 161409(R) (2014).

[24] J. Theilhaber, *Ab initio* simulations of sodium using time-dependent density-functional theory, Phys. Rev. B **46**, 12990 (1992).

[25] A. Castro, M. Marques, and A. Rubio, Propagators for the time-dependent Kohn-Sham equations, J. Chem. Phys. **121**, 3425 (2004).

[26] S. Meng and E. Kaxiras, Real-time, local basis-set implementation of time-dependent density functional theory for excited state dynamics simulations, J. Chem. Phys. **129**, 054110 (2008).

[27] C. Lian, M. Guan, S. Hu, J. Zhang, and S. Meng, Photoexcitation in solids: First-principles quantum simulations by real-time tddft, Adv. Theory Simul. **1**, 1800055 (2018).

[28] E. Luppi, H. Hübener, and V. Véniard, *Ab initio* second-order nonlinear optics in solids: Second-harmonic generation spectroscopy from time-dependent density-functional theory, Phys. Rev. B **82**, 235201 (2010).

[29] C. Attaccalite and M. Grüning, Nonlinear optics from an *ab initio* approach by means of the dynamical berry phase: Application to second- and third-harmonic generation in semiconductors, Phys. Rev. B **88**, 235113 (2013).

[30] P. Garcia-Goiricelaya, J. Krishna, and J. Ibañez-Azpiroz, Including many-body effects into the Wannier-interpolated quadratic photoresponse tensor, Phys. Rev. B **107**, 205101 (2023).

[31] C. D. Pemmaraju, F. D. Vila, J. J. Kas, S. A. Sato, J. J. Rehr, K. Yabana, and D. Prendergast, Velocity-gauge real-time TDDFT within a numerical atomic orbital basis set, Comput. Phys. Commun. **226**, 30 (2018).

[32] P. Li, X. Liu, M. Chen, P. Lin, X. Ren, L. Lin, Y. Chao, and L. He, Large-scale *ab initio* simulations based on systematically improvable atomic basis, Comput. Mater. Sci. **112**, 503 (2016).

[33] M. Chen, G.-C. Guo, and L. He, Electronic structure interpolation via atomic orbitals, J. Phys.: Condens. Matter **23**, 325501 (2011).

[34] J. P. Perdew, K. Burke, and M. Ernzerhof, Generalized gradient approximation made simple, Phys. Rev. Lett. **77**, 3865 (1996).

[35] M. Schlipf and F. Gygi, Optimization algorithm for the generation of ONCV pseudopotentials, Comput. Phys. Commun. **196**, 36 (2015).

[36] D. R. Hamann, Optimized norm-conserving Vanderbilt pseudopotentials, Phys. Rev. B **88**, 085117 (2013).

[37] S. Grimme, J. Antony, S. Ehrlich, and H. Krieg, A consistent and accurate *ab initio* parametrization of density functional dispersion correction (DFT-D) for the 94 elements H-Pu, J. Chem. Phys. **132**, 154104 (2010).

[38] X. Li, J. C. Tully, H. B. Schlegel, and M. J. Frisch, *Ab initio* ehrenfest dynamics, J. Chem. Phys. **123**, 084106 (2005).

[39] R. Fei, L. Z. Tan, and A. M. Rappe, Shift-current bulk photovoltaic effect influenced by quasiparticle and exciton, Phys. Rev. B **101**, 045104 (2020).

[40] J. Krishna, P. Garcia-Goiricelaya, F. de Juan, and J. Ibañez-Azpiroz, Understanding the large shift photocurrent of WS_2 nanotubes: A comparative analysis with monolayers, Phys. Rev. B **108**, 165418 (2023).

[41] C. Pemmaraju, Valence and core excitons in solids from velocity-gauge real-time TDDFT with range-separated hybrid functionals: An LCAO approach, Comput. Condens. Matter **18**, e00348 (2019).

[42] L. Reining, V. Olevano, A. Rubio, and G. Onida, Excitonic effects in solids described by time-dependent density-functional theory, Phys. Rev. Lett. **88**, 066404 (2002).

[43] F. Sottile, V. Olevano, and L. Reining, Parameter-free calculation of response functions in time-dependent density-functional theory, Phys. Rev. Lett. **91**, 056402 (2003).

[44] Y. Li, J. Fu, X. Mao, C. Chen, H. Liu, M. Gong, and H. Zeng, Enhanced bulk photovoltaic effect in two-dimensional ferroelectric $CuInP_2S_6$, Nat. Commun. **12**, 5896 (2021).